International Journal of Thin Films Science and Technology

http://dx.doi.org/10.18576/ijtfst/050101

Simulating Effect of Ferroelectric Nanofiller Shape on Charge Transport in Nanocomposite Film

Meng H. Lean and Wei-Ping L. Chu*

QEDone LLC, Santa Clara, CA 95054 USA.

Received: 15 Sep. 2015, Revised: 24 Nov. 2015, Accepted: 2 Dec. 2015.
Published online: 1 Jan. 2016.

Abstract: Bipolar charge injection and field-dependent mobility transport through nanocomposite film comprised of various shapes of ferroelectric nanofillers in an amorphous polymer matrix is simulated using a self-consistent 3D particle-in-cell model. The classical electrical double layer is extended by substitution of a dipolar core for the nanofiller. Metal-polymer charge injection assumes Schottky emission and Fowler-Nordheim tunneling, migration with field-dependent Poole-Frenkel mobility, and recombination with Monte Carlo selection. A boundary integral equation method solves the Poisson equation coupled with a second-order predictor-corrector scheme for time integration of the equations of motion. The stability criterion of the explicit algorithm conforms to the Courant-Friedrichs-Levy limit. Simulation results for $BaTiO_3$ nanofiller in amorphous polymer matrix indicate that anti-parallel polarization results in the highest leakage conduction and lowest level of charge trapping in the interaction zone. Charge attachment to nanofillers is increased with spheroids due to the increase in surface area, and especially so for anti-parallel polarized oblate spheroids, showing the influence of orientations that present larger cross-sections.

Keywords: nanocomposites, nanofillers, ferroelectric, polymer binder.

1 Introduction

Ceramic nanofillers are incorporated within amorphous polymer binders to result in nanocomposite films for use in energy storage for rapid power cycling applications. Some advantages include: high energy density, low materials and replacement cost, and self-healing, lightweight, and small footprint properties. Nanocomposite films may be engineered to low dielectric loss while combining the processability and high breakdown field strength of the polymer with the high dielectric constant of the fillers. Large contrast in permittivity between the two phases may give rise to highly inhomogeneous electric fields (**E**) in the "interaction zone", defined as the interfacial region that surrounds the nanofillers and interspaces.

Highly inhomogeneous fields and structural inhomogeneity generally lead to a significant reduction in the effective breakdown field strength of the composite, limiting the increase in the energy storage capacity and energy density. Improved dispersion of filler in the polymer matrix create effective electron scattering and transport centers, thus reducing breakdown probability by blocking degradation tree growth and increasing long-term breakdown strength [1]. Polymers currently used as matrices in the dielectric nanocomposites include poly(vinylidene fluoride) (PVDF)-based ferroelectric semicrystalline polymers which exhibit large spontaneous polarization and high dielectric constants (~10 at 1 kHz) because of the presence of highly electronegative fluorine on the polymer chains and the spontaneous alignment of C–F dipoles in the crystalline phases [2]. Considerable progress has been made over the past several years in the enhancement of the energy densities of the polymer nanocomposites by tuning the chemical structures of ceramic fillers and polymer matrices and engineering the polymer-ceramic interfaces. The incorporation of the TiO_2 nanoparticles into the polymer induces an improved electric displacement, which accounts for high energy densities observed in the nanocomposites [3].

Surface hydroxylation treatment using hydrogen peroxide to modify the surface of $BaTiO_3$ (BT) nanofillers dispersed in a ferroelectric copolymer host has resulted in up to two orders of magnitude reduction in the leakage current of nanocomposite thin-film capacitors. This reduction is observed concurrently with the enhancement of effective permittivity and breakdown strength of the thin-film nanocomposites [4]. The challenge in matching nanofillers with the polymer matrix is to understand the role of the interaction zone where the very large area to volume ratio of the interfaces in nanocomposites would have significant

*Corresponding author E-mail: mhlean@ieee.org

impact on the electrical and dielectric properties of the film. Charge mapping studies may help to define and quantify the taxonomy of the mobile, trapped, bound, and polarization charge types and their abundance. Knowledge of the spatial and temporal distributions may facilitate insight into the dynamics of charge re-distributions which lead to breakdown at high fields or prolonged usage. Empirical methods using pulse electroacoustic (PEA) and laser induced pressure pulse (LIPP) techniques have demonstrated preliminary feasibility [5,6]. 1D bipolar charge transport models capable of handling leakage current up to pre-breakdown levels have been successfully applied to layered polymer films [7,8,9]. Axisymmetric models capable of handling divergent field configurations have been reported [10,11].

However, continuum charge transport models are not suited to simulate material with morphology at the nanometer length scale. Commercial software has been used to compute effective permittivity of nanocomposites [12,13]. Several models of nanoparticles are discussed in the literature, including the Tanaka Multicore 3-layer and the Lewis models [14]. The classical electrical double layer (EDL) is similar to the Lewis model and is predicated on a monopole net charge for the core. Charge transport is enabled by the increase in nanoparticle loading within the dielectric composite eventually leading to overlap of the diffuse double layers forming conduction paths. Bulk charge accumulation is reduced due to this internal conductivity, and the dielectric breakdown strength of the nanocomposite is improved.

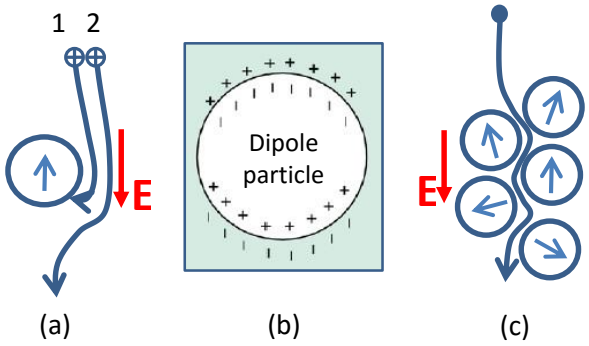

Figure 1: Extended EDL (*eEDL*) model for ferroelectric nanofillers (e.g. $BaTiO_3$) in amorphous polymer (e.g. PVDF) matrix: (a) Initial charge '1' attach to opposite-signed end of dipole particle repel subsequent particle '2' after charge build-up; (b) Maxwell-Wagner-Sillas (MWS) polarization effect; and (c) Charge particle trajectory meandering through inter-spaces.

This paper extends the EDL (*eEDL*) to model ferroelectric nanofillers as shown in Figure 1 where the core is replaced by a dipole of the appropriate physical diameter and dipole moment with assigned orientation. Metal-polymer charge injection assumes Schottky emission and Fowler-Nordheim tunneling, migration through field-dependent Poole-Frenkel mobility, and recombination with Monte Carlo selection. A boundary integral equation method is used for solution of the Poisson equation coupled with a second-order predictor-corrector scheme for robust time integration of the equations of motion. The stability criterion of the explicit algorithm conforms to the Courant-Friedrichs-Levy (CFL) limit. Charge passage may be illustrated in Figure 1(a), where incoming positive charge is repelled by the positive-end and attracted towards the negative-end of the dipole and vice-versa. Charge is allowed to attach on impact forming the bound Stern-Helmholtz layer. Subsequent waves of incoming charge may be repelled to form the diffuse outer Gouy-Chapman transport layer. The cumulative charge buildup on opposing ends of the dipole leads to Maxwell-Wagner-Sillars (MWS) polarization as shown in Figure 1(b). The gradual charge deposition and formation of the diffuse layers as charge migrates through the polymer film creates the interaction zone. Trajectories for charges that make it through the film to the counter-electrode are curvilinear paths that meander through the interspaces, as shown in Figure 1(c). Charges that arrive at the counter-electrode are neutralized and therefore contribute to the conduction of the film; but not to the field. One question that needs to be addressed is the effect of nanofiller shape on charge transport and its implications to nanocomposite energy storage application. This paper will predict bipolar charge injection, transport, and recombination/electroluminescence through nanocomposite film comprising ferroelectric BT nanofiller in amorphous PVDF polymer matrix for various polarizations and for several nanofiller shapes; including spheres and prolate and oblate spheroids.

2 Problem Formulation

2.1. Electrostatic Fields

The composite field due to the bias voltage, space charge, and polarization charge is given by:

$$\boldsymbol{E} = \boldsymbol{E}_{bias} + \boldsymbol{E}_q + \boldsymbol{E}_{dipole} \tag{1}$$

When the particle count, *n*, is small to moderate, fields from the space charge are computed from superposing or summing the point source solutions for all particles considered:

$$\boldsymbol{E}_q = -\int_{V'} \nabla G \frac{1}{\varepsilon_0} \rho(v')\, dV' \approx \sum_{i=1}^{n} \nabla G \frac{1}{\varepsilon_0} q_i \tag{2}$$

With G as the Green function fundamental solution to a point charge in the volume V'. The polarization, **P**, from sphere-shaped ferroelectric materials in a dielectric medium may be written as:

$$\boldsymbol{P} = 3\frac{\varepsilon-1}{\varepsilon+2}\boldsymbol{E} \tag{3}$$

Where ε is the ratio of the permittivity of the sphere to the

polymer matrix, and (ε–1)/(ε+2) is the Clausius-Mossotti factor which vanishes when the material and medium permittivities are identical. The material component of the dipole moment given by:

$$\boldsymbol{p_{CM}} = \frac{4}{3}\pi a^3 \boldsymbol{P} = 4\pi \frac{\varepsilon-1}{\varepsilon+2} a^3 \boldsymbol{E} \tag{4}$$

Is summed with the intrinsic dipole moment to compute the net dipole field as:

$$\boldsymbol{E}_{dipole} = -\frac{1}{4\pi\varepsilon_0}\left(\frac{3(\boldsymbol{p}\bullet\boldsymbol{r})\boldsymbol{r}-\boldsymbol{p}}{r^3}\right) \tag{5}$$

Where $\boldsymbol{p}$, is the net dipole moment, r is the distance of evaluation, and a is the nanofiller radius.

The solution of the Poisson equation is obtained using the boundary integral equation method (BIEM), based on the use of the free space Green function as the solution to a point source. Instead of the classical approach to derive a particular Green function that incorporates geometry, material properties, and boundary conditions, linearity and superposition is invoked to solve an equivalent (and simpler) problem. The source distribution technique (SDT) treats mobile space charge and bulk trapped charge as volume sources, and replaces conducting boundaries and material interfaces with appropriate distributions of unknown free and bound interfacial polarization and trapped charges to satisfy the specified boundary and interface conditions. Enforcement of boundary conditions for potential and flux and interface conditions at material interfaces for continuity of tangential **E** and normal **D** (=ε**E**):

$$\boldsymbol{n} \times (\boldsymbol{E}_1 - \boldsymbol{E}_2) = 0 \tag{6}$$

$$\boldsymbol{n}\bullet(\varepsilon_1\boldsymbol{E}_1 - \varepsilon_2\boldsymbol{E}_2) = \frac{\lambda}{\varepsilon_0}$$

For the Poisson equation result in

$$\int_{S'} G\frac{\sigma(s')}{\varepsilon_0}dS' + \int_{C'} G\frac{\gamma(c')}{\varepsilon_0}dC' = \phi(s) - \int_{V'} G\frac{\rho(v')}{\varepsilon_0}dV' \tag{7}$$

$$\left\{\int_{S'} \frac{\partial G}{\partial n}\frac{\sigma(s')}{\varepsilon_0}dS' - \frac{\sigma(s)}{2\varepsilon_0}\right\} + \int_{C'} \frac{\partial G}{\partial n}\frac{\gamma(c')}{\varepsilon_0}dC' = \frac{\partial\phi(s)}{\partial n} - \int_{V'} \frac{\partial G}{\partial n}\frac{\rho(v')}{\varepsilon_0}dV' \tag{8}$$

$$\left\{\int_{C'} \frac{\partial G}{\partial n}\frac{\gamma(c')}{\varepsilon_0}dC' - \frac{\varepsilon_1+\varepsilon_2}{\varepsilon_1-\varepsilon_2}\frac{\gamma(c)}{2\varepsilon_0}\right\} + \int_{S'} \frac{\partial G}{\partial n}\frac{\sigma(s')}{\varepsilon_0}dS' = -\frac{\lambda(c)}{\varepsilon_0(\varepsilon_1-\varepsilon_2)} - \int_{V'} \frac{\partial G}{\partial n}\frac{\rho(v')}{\varepsilon_0}dV' \tag{9}$$

For Dirichlet, Neumann, and dielectric interface conditions, respectively, where ϕ(s) and ∂ϕ(s)/∂n are the potential and normal derivative on the surface. Selective enforcement at collocation points generate discretized equations that result in a matrix that is inverted to determine the magnitude of the free and bound polarization source distributions. Then fields and field derivatives are computed by integrating contributions from all the source distributions. Kernel functions, including the Green function and its analytic derivatives (G, ∂G/∂n, and ∇G) are integrated numerically using Gauss-Legendre quadrature. Singular kernels are accurately computed using minimum order sampling by tying the quadrature weight function to the singularity. Details on the computation of these integrals are discussed in detail for axisymmetric and 2D geometries.[13,15] Discretized forms of these three equations are solved simultaneously for σ(s) on electrodes and γ(c) on interfaces. Equations (7) to (9) invoke superposition of sources that include: free charge, σ, on electrodes (S'); polarization charge, γ, and trapped charge, λ, on material and physical interfaces (C'); and mobile and trapped space charge, ρ in the volume (V'). Free charge at the two electrode-polymer interfaces and polarization and trapped charge at the polymer-polymer interface are related to the electric fields on sides *1* and *2* by:

$$\begin{aligned}\sigma_{electrode} &= \varepsilon_0\varepsilon_r \boldsymbol{n}\bullet\boldsymbol{E} \\ \sigma_{polarization} &= \varepsilon_0(\boldsymbol{n}\bullet\boldsymbol{E}_2 - \boldsymbol{n}\bullet\boldsymbol{E}_1) \\ \sigma_{trapped} &= \varepsilon_0(\varepsilon_2\boldsymbol{n}\bullet\boldsymbol{E}_2 - \varepsilon_1\boldsymbol{n}\bullet\boldsymbol{E}_1)\end{aligned} \tag{10}$$

Therefore allowing direct inference of the **E** fields. Elements of the discretized matrices on the left hand sides of (7) to (9) are calculated from spatial integrals and therefore need not be recomputed for every time-step. Large portions of the matrices may be saved and reused in matrix algebra for rapid computation of the sources, or independent variables, σ andγ. The forcing functions on the right hand side may be approximated as summations of discrete contributions from point charges as shown in (2). More details on this charge taxonomy and the use of rapid matrix algebra are reported in the literature [15].

With A as electrode area, and J as the current density defined in (19), finite numbers of positive and negative charge particles, Δn, are injected at each time-step, Δt, from the cathode and the anode into the respective adjacent polymer according to:

$$\Delta n = \frac{JA}{q}\Delta t \tag{11}$$

Where the charges are injected from randomized locations on the surface of the corresponding electrodes.

For large numbers of particles, n, and spatially varying distributions a "scatter-gather" method may be used to scatter the space charge,ρ, to q_i on the vertices of the inscribed volume mesh using, for example, trilinear interpolation:

$$\rho = \frac{\sum_{i=1}^{8}\alpha_i q_i}{V} \tag{12}$$

Where α_i are the trilinear interpolation functions and V is the mesh volume. This particle-mesh scheme facilitates integration by gathering the contributions from the vertices, i, of all volume meshes, j:

$$\boldsymbol{E} = \int_{V'} \nabla G \rho(v') \frac{1}{\varepsilon_0} dV' \approx \sum_{j=1}^{k} \sum_{i=1}^{8} \nabla G \frac{1}{\varepsilon_0} \alpha_i q_i \quad (13)$$

To compute the **E** field at the ρ position. This method requires only nk ($<<n^2$) calculations for a mesh of size $k<<n$. Following (12), the current density, $\boldsymbol{J}$, can be similarly expressed as:

$$\boldsymbol{J} = \frac{\sum_i \alpha_i q_i \boldsymbol{v}_i}{V} \quad (14)$$

With $\boldsymbol{v}_i$ (=μ**E**) as the drift velocity. Contributions of these volume sources to the **E**-field are evaluated as the algebraic summations of the field from each volume mesh as shown in (13).

2.2. Equations of Motion

The electrodynamic simulation of space charge migration through the nanocomposite film involves the time-dependent integration of the two equations of motion:

$$m \frac{d\boldsymbol{v}}{dt} = q\boldsymbol{E} \quad (15)$$

$$\frac{d\boldsymbol{x}}{dt} = \boldsymbol{v} \quad (16)$$

Where m and q are the mass and the charge of the particle, v is its velocity and **E** is the electric field at the particle location. The equations above are followed in time as they evolve in velocity and position (phase space) to determine the trajectory of each particle. The driving terms in (15) are the Coulomb and dipole forces. Due to the small acceleration time and short mean free path, implementation of (15) and (16) may be simplified by assuming that charge migrates with a drift velocity, **v**=μ**E**, where μ is the mobility in the polymer.

3 Simulation Algorithm

3.1. Particle Simulation

Solution of the Poisson equation for charge conservation and integration of the equations of motion at each time interval form a two-step field solve-particle push algorithm for particle simulation in the computational cell. Nanofillers are randomly distributed within the cell to the prescribed vol.% loading using "hard sphere" logic; i.e. allowing contact but no over-lap. The 3D PIC model tracks the dynamics of charge particle injection, particle-particle interactions, and particle attachment to nanofillers during migration through the amorphous polymer and nanocomposite layers between the top and bottom electrodes. The self-consistent **E** field solution is obtained using the BIEM. Particle tracking involves a predictor-corrector algorithm to integrate the equations of motion subject to the applied bias. A self-consistent particle-particle, particle-mesh (P^3M) scheme may be implemented for very large numbers of particles [16-18].

3.2. Computational Cell

The computational cell used for the nano-scale simulations is shown in Figure 2 where the 500 nm nanocomposite layer is sandwiched between two 250 nm amorphous polymer layers. The cell is a cuboid of edge dimension 1 μm, volume of 1 μm^3, bounded by 4 vertical side walls with zero flux condition ($\partial\phi/\partial n = 0$), and top (anode) and bottom (cathode) electrodes at constant potential to maintain the bias **E** field. Discrete numbers of charge particles, dictated by the current density and time-step, are continuously injected from the electrodes as a function of the averaged electrode **E** field. Injection locations are randomly dispersed over the electrode surface. Charge particles migrate through the nanofiller distribution under the composite **E** field with those arriving at the counter-electrode considered neutralized and therefore having no further contribution to the **E** field. Periodic boundary conditions imposed on the 4 vertical walls force exiting particles to re-enter at the opposite side walls.

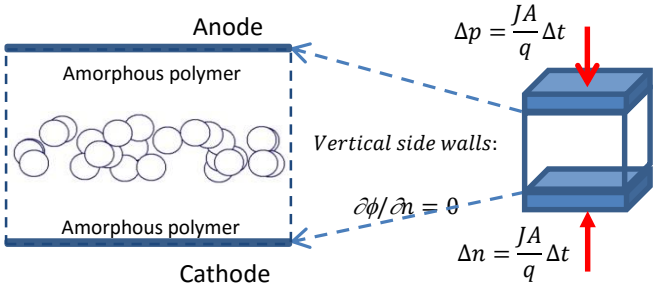

Figure 2: Side view of computational cell with 500 nm nanocomposite layer sandwiched between 250 nm layers of amorphous polymer in a cubic cell of volume 1 μm^3 with vertical side walls as zero flux boundaries and electrodes as charge injectors.

To minimize local error, displacement, Δh, is required to be smaller than the Debye length, i.e. $L_D=(\varepsilon k_B T/q^2 N_i)^{½}$, where N_i is the largest charge number density. The time step, Δt, needs to be shorter than the dielectric relaxation time, $\tau=\varepsilon/qN_i\mu$, characteristic of charge fluctuations to decay. The stability criterion of the explicit algorithm is given by the CFL limit, c:

$$c = \left|\frac{v\Delta t}{\Delta h}\right| \leq 1 \quad (17)$$

which represents the ratio of mobile charge velocity, v, to trace velocity, $\Delta h/\Delta t$. For stability, (17) states that the trace velocity cannot be faster than the speed of the charge [19].

3.3. Time Integration

The two differential equations given by (15) and (16) are integrated numerically using a predictor-corrector method of order Δt^2, or second-order accurate in time. The dependent variable, $\boldsymbol{x}$, is iteratively improved at each time level. To start, we assume that at time level n, the set ($\boldsymbol{x}^{n-1}$,

$\boldsymbol{x}^n$) is known. Then, the predictor-corrector equations are:

Predictor:

$$\boldsymbol{v}^n = \boldsymbol{\mu}\boldsymbol{E}^n$$
$$\boldsymbol{x}^{n+1} = \boldsymbol{x}^{n-1} + 2\Delta t\, \boldsymbol{v}^n$$
$$\boldsymbol{x}^{n-1\prime} = \boldsymbol{x}^n + \tfrac{1}{4}(\boldsymbol{x}^{n+1} - \boldsymbol{x}^{n-1})$$

Corrector:

$$\boldsymbol{v}^{n+1} = \mu\boldsymbol{E}^{n+1} \quad (18)$$
$$\boldsymbol{x}^{n+1} = \boldsymbol{x}^{n-1\prime} + \frac{1}{2}\Delta t\, \boldsymbol{v}^{n+1}$$

Update:

$$\boldsymbol{x}^{n-1} = \boldsymbol{x}^n$$
$$\boldsymbol{x}^n = \boldsymbol{x}^{n+1}$$

In the predictor stage, the initial location for the (*n-1*) iteration level is improved and used in the corrector stage to obtain the updated location for the next time level. The above tacitly assumed that the field is "frozen-in" relative to the time step of charge migration, and the transient time to attain terminal velocity is much shorter than the mean free path or the time between collision events of oppositely charged particles.

4 Bipolar Charge Transport

4.1. Charge Injection

At low to moderate applied fields, charge injection from a metal electrode into the lowest unoccupied molecular orbital (LUMO) band of the polymer by Schottky barrier thermionic emission is given by:

$$J_n = AT^2 e^{-\frac{(W_n - \Delta w)}{k_B T/q}} \quad (19)$$
$$J_p = AT^2 e^{-\frac{(W_p - \Delta w)}{k_B T/q}}$$

Where A is the Richardson constant (=1.2×10^6 A/m^2.K^2), and W_n and W_p are the energy barriers to injection in eV. The combined effect of the image force and the applied field results in a lowering of the barrier potential given by:

$$\Delta w = \sqrt{\frac{qE}{4\pi\varepsilon}} \quad (20)$$

At higher applied fields, the slope gets steeper and the barrier is further lowered so that the tunneling length is much shorter, increasing the probability for tunneling through the barrier. Charge injection from a metal electrode into the polymer is treated using the Fowler-Nordheim quantum mechanical tunneling model given by:

$$J = CE^2 e^{-\frac{\beta}{E}} \quad (21)$$

Where C = ($q^3/16\pi^2 h\Phi_e$), $\beta = (4\sqrt{2m_e}/3hq)\Phi_e^{3/2}$, m_e is the electron effective mass, h is Planck's constant (4.1356×10^{-15} eV.s), and Φ_e is the effective potential barrier. Φ_e is equal to qW_p or qW_n for positive and negative charge, respectively. For the set of simulation parameters used here, the transition from Schottky emission to Fowler-Nordheim tunneling occurs at about 166 V/μm [9].

4.2. Field-dependent Mobility

At low-fields and low densities, carriers are almost in equilibrium with the lattice vibrations so the low-field mobility is mainly affected by phonon and Coulomb scattering. The mobility increases until the velocity approaches the random thermal velocity. In a moderately large electric field, less thermal fluctuation is required to free charge allowing for higher conduction via the Poole-Frenkel mobility:

$$\mu = \mu_0 e^{\gamma\sqrt{E}} \approx \mu_0 e^{\left(\frac{\Delta w}{k_B T/q}\right)} \quad (22)$$

Where γ is a constant, and Δw is as defined in (20). At higher electric fields, mobility decreases with increasing electric field due to increased lattice scattering at higher carrier energies, and carrier velocity saturate. The Caughey-Thomas field-dependent mobility:

$$\mu = \frac{\mu_0}{\left[1+\left(\frac{\mu_0 E}{v_{sat}}\right)^{\beta}\right]^{1/\beta}} \quad (23)$$

Provides a smooth transition between low-field and high field behavior where μ_o is the low field mobility at a field of E_o, v_{sat} is the saturation velocity, and β=1 is commonly used [20].

4.3. Charge Attachment/Detachment

Trapping and de-trapping of space charge in polymeric materials are related to the microstructure and morphology of the materials. Analogous to the continuum model, trapped charge on nanofiller surfaces are considered to be attached charge. In the *eEDL* model, initial charge attachment to nanofillers are assumed to be deterministic, i.e. attachment on impact, or probability $P_t(t)=1$. Subsequent taper-off due to Coulomb force and dipole field repulsion from build-up of the attached charge follow the MWS effect, i.e. $P_t(t)\rightarrow 0$ as the limiting behavior. Charge detachment, to be considered in future model development, may be physically controlled by comparing the local field to the trap depth used in the de-trapping rate, k_d, equation:

$$k_d = N_c \upsilon_{th} \sigma e^{-E_t/k_B T} \quad (24)$$

Where N_c is the effective density of states in the LUMO, v_{th} is the thermal velocity, and E_t is the trap depth [9].

4.4. Recombination

The Monte Carlo collision model is used to describe particle-particle events between oppositely charged entities

resulting in recombination [17]. The probability of a collision of the i^{th} charge particle with a charge particle of the opposite polarity in a time step Δt is given by:

$$P_i = 1 - e^{-n_0 \sigma(E_i) v_i \Delta t} \quad (25)$$

where n_0 is the number density of the opposite polarity mobile charge, $\sigma(E_i)$ is the total collision cross-section which in general depends on the kinetic energy of the i^{th} particle (could be larger than the geometrical cross-section given by $\sigma = \pi(r_i + r_j)^2$), and v_i is the velocity of this particle relative to the velocity of the opposite polarity particle. Therefore, $n_o\sigma$ is a measure of the number of collisions per unit length, $1/n_o\sigma$ is the mean free path between collisions, and $n_o\sigma v_i$ is the collision frequency. For a finite Δt, the probability of a collision is determined by comparing P_i with R_i, representing a uniform random number between 0 and 1. For $P_i > R_i$, the particle i is assumed to have sustained a collision within the time step Δt resulting in recombination and neutralization of the charge pair. Otherwise, Monte Carlo selection returns a non-event.

5 Results and Discussion

The model for the nanocomposite film is a random distribution of nanofillers in a 500 nm layer sandwiched on the top and bottom by 250 nm amorphous polymer layers. Only unipolar injection from the anode is considered here to allow clearer illustration of results. Charge transport studies are performed for several nanoparticle polarization orientations with respect to the bias **E** field, including: random, in-plane, parallel, and anti-parallel as shown in Figure 3. Table 1 summarizes the simulation parameters, and includes the dipole moment of BT nanofillers [21].

Table 1: Simulation Parameters.

Parameter	Value	Description
μ_p	9 x 10^{-11} cm^2/V.s	Mobility of positive charge
μ_n	9 x 10^{-11} cm^2/V.s	Mobility of negative charge
W_p	1.2 eV	Anode barrier potential
W_n	1.2 eV	Cathode barrier potential
ε_{PVDF}	12.4	Dielectric constant of PVDF
ε_{BT}	1000.	Dielectric constant of $BaTiO_3$
d_{BT}	50 to 150 nm	Diameter of $BaTiO_3$
m_{BT}	4.25x10^{-30} C.m	Dipole moment of $BaTiO_3$

Results are generated for a comparative study of shape dependence of the BT nanofiller (which may also be other Perovskites such as TiO_2, or ZrO_2) on charge transport. Nanofiller shapes are constrained to have identical volumes, and include the sphere, prolate spheroid, and oblate spheroid.

In particular, the prolate spheroid and oblate spheroid are arbitrarily chosen to have c/a=4 and c/a=1/4, respectively, where c and a are the semi-major and semi-minor axes. Table 2 contains the dimensions and surface areas for a volume defined by a 150 nm spherical nanoparticle.

Table 2: Spheroid Parameters.

Spheroids	a <nm>	c <nm>	r <nm>	Norm* Surface Area
Sphere	–	–	75.00	1.00
Prolate	47.25	188.99	–	1.28
Oblate	119.06	29.76	–	1.43

a, c – semi-minor, -major axes; *surface area normalized to sphere

Sample trajectories are shown in Figure 4 for randomly distributed 150 nm nanofillers (large circles) at 10 vol.% loading with dipole moment of 4.25x10^{-30} C.m and in-plane, parallel, and anti-parallel polarization. Figure 4(a) for in-plane polarization shows the rear view with 7 attachments and 3 trajectories passing through to the counter-electrode, one of which suffers multiple deflections enroute. The side view in Figure 4(b) shows 8 trajectories terminating on upper half-spheres due to the bias field and the added attraction of the dipole field, and 2 passing through to the counter-electrode completing a conduction event. Finally, Figure 4(c) contains a perspective view showing trajectories terminating on the tail-end of the spheres and 1 trajectory that is repelled by the front-end of the dipole, deflected laterally, and subsequently moving to the counter-electrode.

Figures 5(a) and 5(b) show the charge fractions, normalized to total charge, of those attached to spherical nanofillers and those that arrived at the counter-electrode for the 4 polarization cases. The time axes indicate the transit times for charge to travel to the nanofiller and through to the counter-electrode. Lower attachment results in higher conduction or higher fractions of arrivals at the counter-electrode, and vice-versa. In all runs, the tracking time is adjusted so that the same amount of charge is injected.

The random and in-plane cases have similar results with the latter case exhibiting a slightly higher attachment due to all dipoles being aligned in the plane to provide equal access to the opposite-signed ends. The parallel case presents the negative end of the dipoles directly to the positive charge and results in the highest attachment. The anti-parallel case is just the opposite, making it more difficult for incoming positive charge to be initially repelled before they can be drawn to the underside of the dipoles. Depending on the proximity of the neighboring nanoparticles, a dipole polarization cancellation effect may cause the charge particle to continue migration therefore increasing the probability of propagating through to the counter-electrode.

In particular, for the anti-parallel case, very little attachment is observed to the nanofillers with > 90% arrival at the counter-electrode.

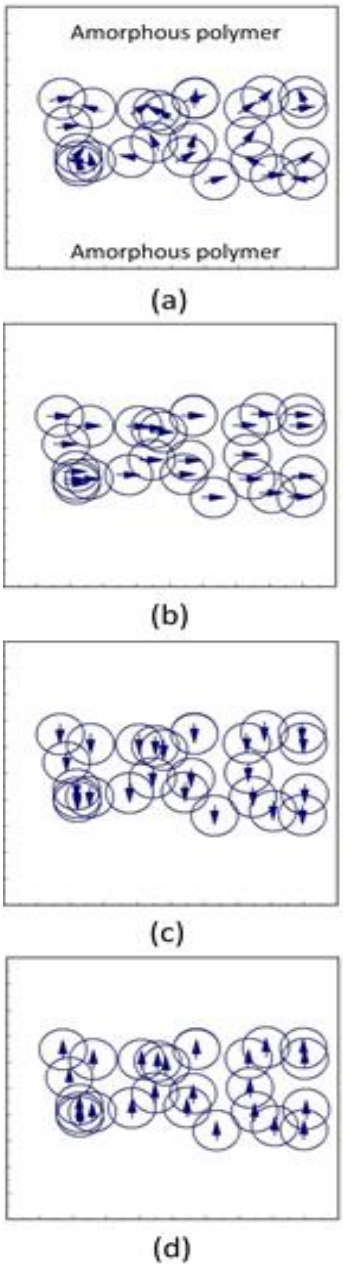

Figure 3: Nanocomposite film with nanofiller polarizations including: (a) random; (b) in-plane; (c) parallel; and (d) anti-parallel with respect to the bias **E** field.

Figure 6(a) for 10 vol.% spherical BT nanofillers shows average electrode **E** fields are decreased due to the anti-parallel polarization. The transient time is equivalent to the charge transit time between the electrodes. The slightly lower (negative) average **E** field on the anode is due to the presence of injected positive charge. In Figure 6(b), injected current density at the anode is seen to stabilize after a time interval of 1 transit time.

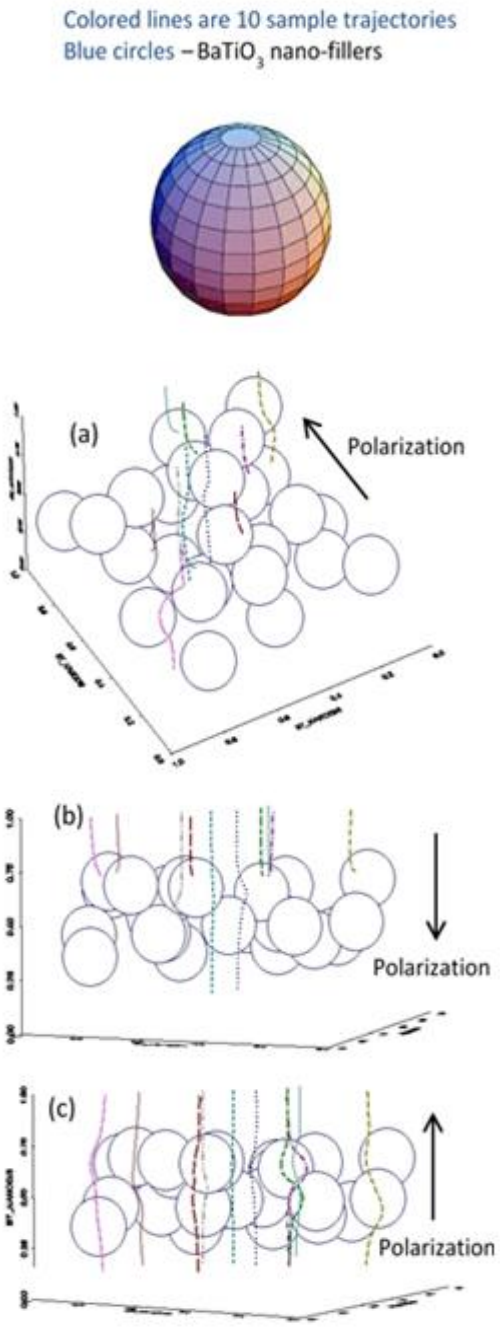

Figure 4: Perspective views of sample trajectories for: (a) in-plane; (b) parallel; and (c) anti-parallel polarizations of randomly distributed 150 nm spherical nanofillers (large circles) at 10 vol.% loading showing attachment and conduction events. Meandering of the tracers indicate the nature of charge migration through the interaction zone formed by the interfaces of the nanofillers and amorphous polymer binder.

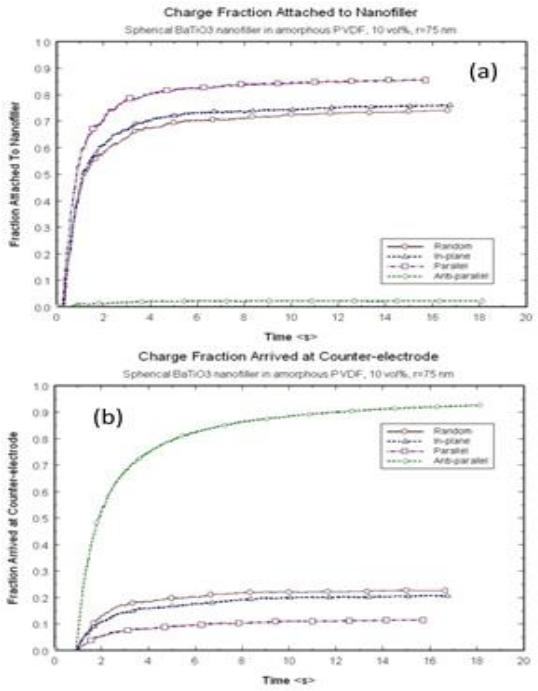

Figure 5: Charge particle fractions: (a) attached to spherical nanofillers; and (b) arrived at the counter-electrode with up to 90% for the anti-parallel case. Time axes show transit times to nanofiller and counter-electrode.

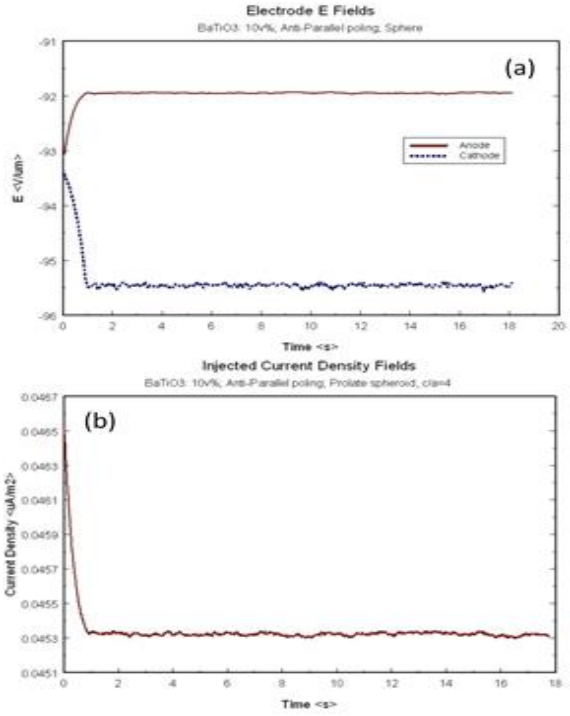

Figure 6: (a) Average anode and cathode **E** fields for 10 vol.% $BaTiO_3$ nanofillers are reduced due to the anti-parallel polarization, with the anode **E** field also lowered by the proximity of the injected positive charge; and (b) Injected current density at the anode stabilizes after 1 transit time.

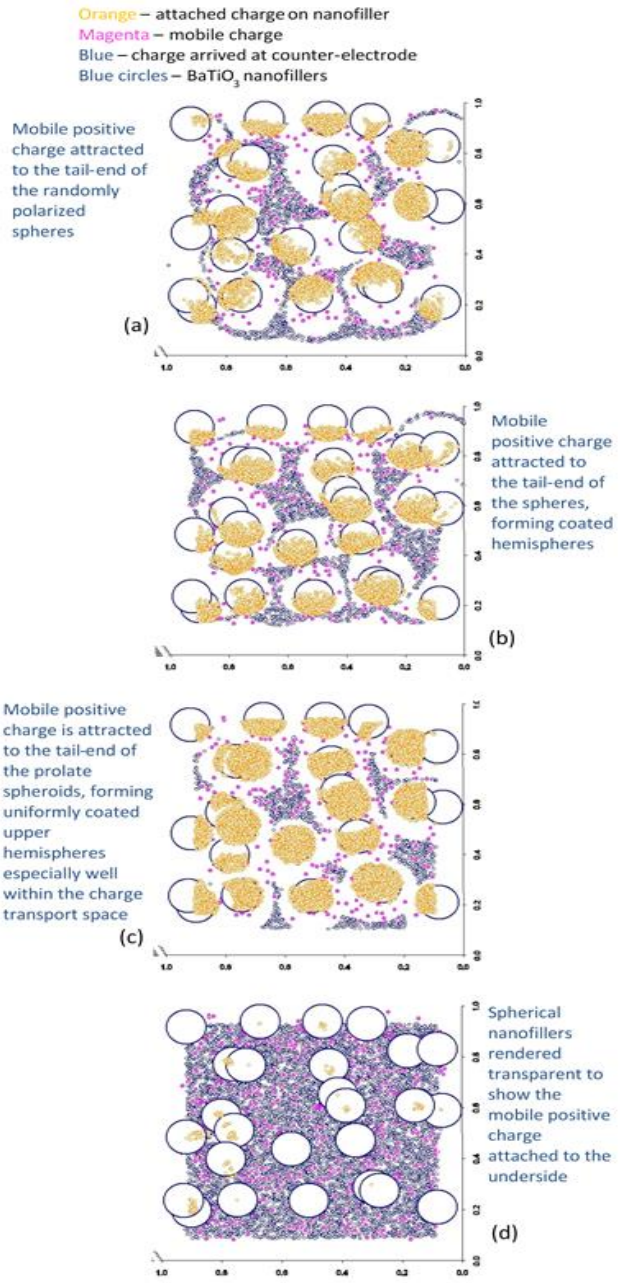

Figure 7: Top views of scatter plots showing randomly distributed 150 nm spherical nanofillers (large circles) at 10vol.% loading and attached charge (orange), mobile charge (magenta), and conduction charge (blue) for: (a) random; (b) in-plane; (c) parallel; and (d) anti-parallel polarizations.

Shown in Figure 7 are the top views of scatter plots for the randomly distributed 150 nm spherical nanofillers (large circles) at 10 vol.% loading and attached charge (orange), mobile charge (magenta), and charge arrived at the counter-electrode (blue) for random, in-plane, parallel; and anti-parallel polarizations. Figure 7(a) shows the mobile positive

charge attracted to the tail-end of the randomly polarized spheres. The upwards-directed in-plane polarization in Figure 7(b) shows attachment to the back end of the spheres. Figure 7(c) shows mobile positive charge attracted to the tail-end of the parallel polarized sphere, forming uniformly coated upper hemispheres. Finally, as seen in Figure 7(d) is the anti-parallel polarized spherical nanofillers rendered transparent to show the mobile positive charge attached to the underside or lower hemisphere.

In Figure 8 are the top views of scatter plots of the randomly distributed 150 nm prolate spheroidal nanofillers (large circles) at 10 vol.% loading and attached charge (orange), mobile charge (magenta), and charge arrived at the counter-electrode (blue) for in-plane, parallel, and anti-parallel polarizations. Figure 8(a) shows the mobile positive charge attracted to the tail-end of the in-plane polarized prolate spheroids. Figure 8(b) also shows the mobile positive charge attracted to the tail-end of the prolate spheroids, forming uniformly coated upper hemispheres. Finally, in Figure 8(c) are shown the prolate spheroidal nanofillers with the mobile positive charge attached to the upper side or upper hemisphere. Note that the attachment to the same-signed dipole end is because the bias field dominates over the repulsion of the dipole field near the tip of the longer semi-major axis when c/a=4.

The top views in Figure 9 are scatter plots of the randomly distributed 150 nm oblate spheroidal nanofillers (large circles) at 10vol.% loading and attached charge (orange), mobile charge (magenta), and charge arrived at the counter-electrode (blue) for in-plane, parallel, and anti-parallel polarizations. Figure 9(a) shows the mobile positive charge attracted to the tail-end of the in-plane polarized oblate spheroids. Figure 9(b) also shows the mobile positive charge attracted to the tail-end of the oblate spheroids, forming fully coated upper hemispheres. Finally, in Figure 9(c) is shown the oblate spheroidal nanofillers with mobile positive charge attached to the upper side or upper hemisphere.

Table 3: Charge fractions for BT in amorphous PVDF.

Sphere	% Mobile	% Attached	% Conduction	Polarization
Random	3.29	74.12	22.59	?
In-plane	3.22	76.14	20.64	→
Parallel	3.10	85.47	11.43	↓
Anti-parallel	5.05	2.24	92.70	↑
Prolate				
In-plane	3.27	73.79	22.95	→
Parallel	3.57	73.11	23.33	↓
Anti-parallel	5.10	10.27	84.63	↑
Oblate				
In-plane	3.39	73.55	23.06	→
Parallel	2.43	91.79	5.78	↓
Anti-parallel	3.63	55.13	41.24	↑

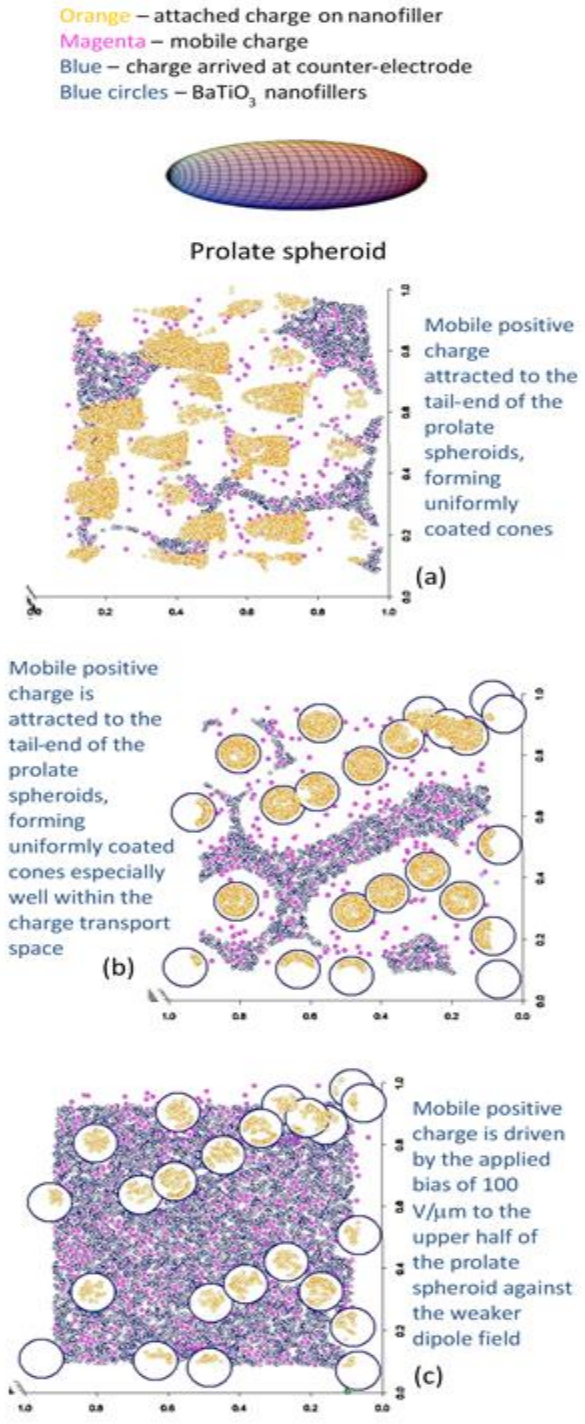

Figure 8: Top views of scatter plots showing randomly distributed 150 nm prolate spheroidal ferroelectric nanofillers at 10vol.% loading and attached charge (orange), mobile charge magenta), and conduction charge (blue) for: (a) in-plane; (b) parallel; and (c) anti-parallel polarizations.

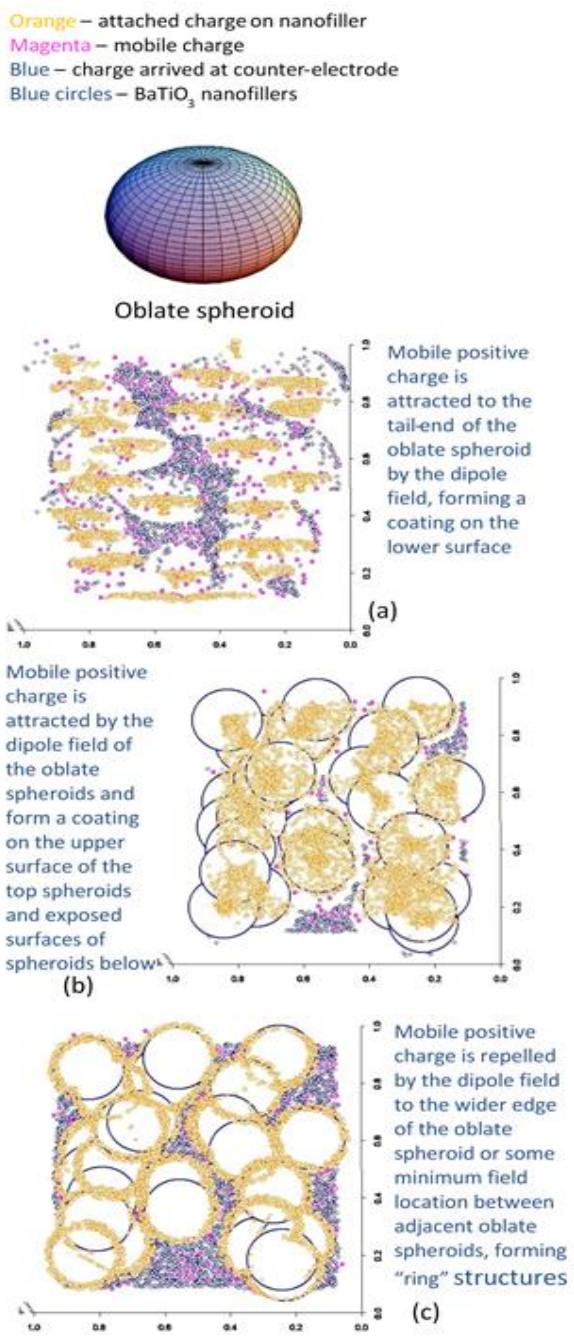

Figure 9: Top views of scatter plots showing randomly distributed 150 nm oblate spheroidal ferroelectric nanofillers at 10vol.% loading and attached charge (orange), mobile charge magenta), and conduction charge (blue) for: (a) in-plane; (b) parallel; and (c) anti-parallel polarizations.

Figure 10(a) shows the fractions of attached, mobile, and conduction positive charge captured on anti-parallel polarized spherical nanofillers where the curves asymptote in time to 2.24%, 5.05%, and 92.70%, respectively, indicating low attachment and high conduction. Corresponding plots for prolate spheroidal nanofillers are shown in Figure 10(b), with the respective curves asymptoting in time to 10.27%, 5.10%, and 84.63%. Similarly, plots for oblate spheroidal nanofillers are shown in Figure 10(c) where the curves asymptote in time to 55.13%, 3.63%, and 41.24%, respectively, with the attached and conduction fractions inverted in the oblate spheroid case.

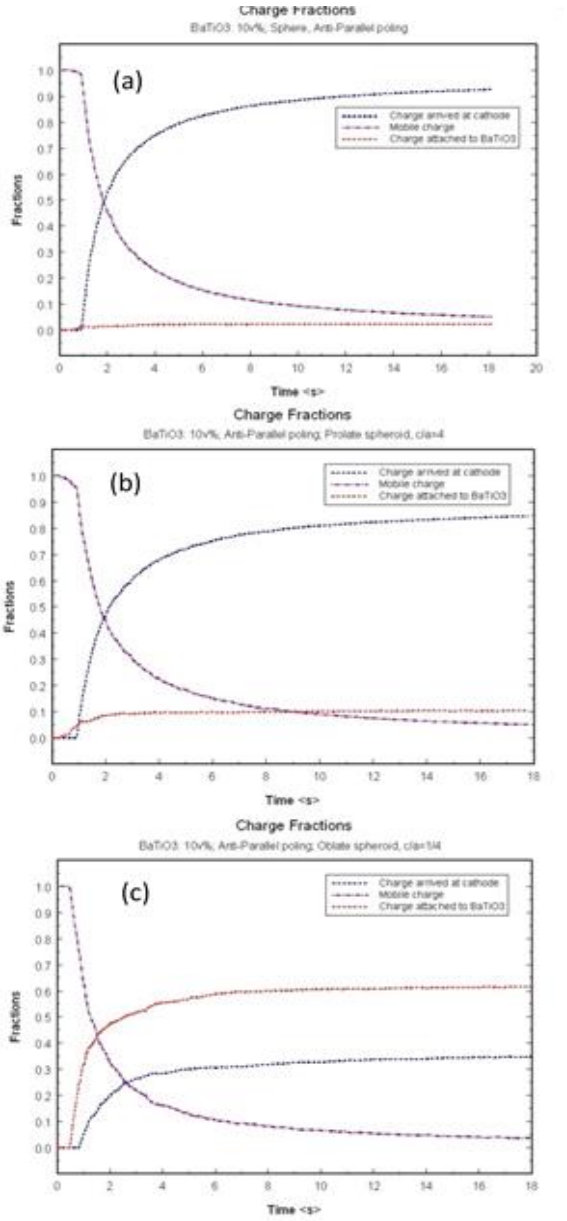

Figure 10: Fractions of attached, mobile, and positive conduction charge for: (a) spherical; (b) prolate spheroidal; and (c) oblate spheroidal shaped nanofillers asymptote with time for any given volume fraction, with the attached and conduction fractions inverted in the oblate spheroid case.

Table 3 summarizes the asymptotes of all charge fractions for all the polarization cases and geometrical shapes. Several observations may be inferred:

- For any shaped nanofiller: (a) parallel polarization results in the highest charge attachment, and therefore lowest conduction, due to the combined effects of the bias field and the attraction of the dipole field; (b) anti-parallel polarization results in the lowest charge attachment, and therefore highest conduction, due to the opposition of the dipole field to the bias field; and (c) in-plane polarization tends to capture slightly more charge than the random case, and therefore have somewhat lower conduction.
- In the anti-parallel case: (a) the mobile charge is repelled before it is attracted to the tail-end; a situation which is repeated as near co-linear dipole fields cancel, thus facilitating continued migration of the charge through the interspaces, thereby increasing conduction; and (b) charge attachment follows the order: oblate > prolate > sphere. Prolate > sphere due to smaller dipole repulsion field at larger *c*. Oblate > sphere because of larger capture cross-section.
- For parallel polarization, charge attachment follows the order: oblate > sphere > prolate due to geometrical cross-section.
- For the prolate spheroid with $c/a=4$, the parallel polarization case involve a longer distance ($c>r$) between the incoming particle and the centroid, thereby minimizing the additive effect of the dipole field on the bias field.

From the preceding results, it is evident that anti-parallel polarization has dramatically higher conduction, a property which has immediate implications to reducing residual charge accumulation and extending the lifetime and reliability of nanocomposite films. Previous studies have determined that in-plane and parallel polarization cases lead to increased attachment and therefore fewer trajectories that form conduction events [22,23]. The opposing **E** field of the anti-parallel polarized nanofiller acts to lower net **E** field, reduce charge injection, and minimize attachment to nanoparticles because the dipole is oriented for field repulsion. An application that benefits from this feature is the increase in power conversion efficiency (PCE) of organic photovoltaic (OPV) devices by inserting an ultrathin film of a ferroelectric co-polymer, P(VDF-TrFE), at the metal–organic interface to enhance the charge extraction efficiency. Highly crystalline P(VDF-TrFE) films prepared by the Langmuir–Blodgett method spontaneously polarize and has been shown to be responsible for the enhancement of PCE in ferroelectric OPV devices [24].

The barrier properties of polymers can be significantly altered by inclusion of nanofillers with large aspect ratio, especially when they are oriented orthogonal to the charge propagation path. Comparing the entries in column 4 of Table 3 for prolate and oblate spheroids with anti-parallel polarization, it is clear that the fraction of charge particles that arrive at the counter-electrode is halved for the current set of parameters. Oriented higher aspect ratio nanofillers may mandate more tortuous pathways for the charge particles to transverse the nanocomposite.

6 Conclusions

This paper has described a rapid 3D particle simulation algorithm which couples the BIEM with robust predictor-corrector time integration of the equations of motion to efficiently simulate bipolar charge transport through nanocomposite polymer film comprised of ferroelectric nanofillers in amorphous polymer matrices. An extended EDL model was implemented which substituted a dipole for the monopole in the classical EDL model. The rationale was to allow for the initial charge particles to attach onto the nanofillers on impact to form the bound Stern-Helmholtz layer. Subsequent charge particles are repelled due to charge build up and the MWS effect, leading to the formation of the diffuse Gouy-Chapman transport layer. Metal-polymer charge injection assumed Schottky emission at low to moderate fields and Fowler-Nordheim tunneling at high fields. Injected particles were migrated via field-dependent Poole-Frenkel mobility and recombined with Monte Carlo selection. A boundary integral equation method was used for solution of the Poisson equation coupled with a second-order predictor-corrector scheme for robust time integration of the equations of motion. The stability criterion of the explicit algorithm conformed to the CFL limit. Careful trajectory tracking revealed the curvilinear paths taken by charge particles that meander through the interspaces that form the interaction zone. Results have substantiated the use of the *eEDL* model for treatment of nanocomposites in bipolar charge transport studies.

A matrix of simulation runs was performed to study the effect of nanofiller shape on bipolar charge transport for random, in-plane, parallel, and anti-parallel polarizations. The anti-parallel polarization results are particularly interesting because of increased leakage conduction and decreased charge attachment to nanofillers; possibly leading to improved reliability and better breakdown strength. The explanation is the preferential attachment of charge to the tail (negative) end of the dipole due to charge polarity. The mobile charge is repelled before it is attracted to the other end; a situation which is repeated as almost co-linear dipole fields of aligned nanofillers cancel, thus facilitating the charge to migrate through the interspaces.

The study of shape-dependence and effects of physical barriers on charge transport shows that both polarization and geometry play contradictory roles. Anti-polarized orientation lowers the electrode **E** field and forces the charge to be initially repelled by each nanofiller particle thus increasing the charge fraction that makes it to the counter-electrode, resulting in higher conduction. Higher aspect ratio geometries, especially if oriented with the larger cross-section orthogonal to the propagation pathways, act to reduce the charge fraction arriving at the counter-electrode, decreasing conduction. Analogies to

flow fields exist where at high aspect ratio in nanocomposites, significant decreases in permeability are predicted and observed in practice [25]. High aspect ratio nanolayers provide properties that are not possible for larger-scaled composites. The impermeable layers mandate a tortuous pathway to transverse the nanocomposite. The enhanced barrier characteristics and lower charge migration are benefits from the hindered diffusion pathways through the nanocomposite.

An area of future work will involve derivation of transport and attachment/detachment coefficients from empirical data on time-dependent I-V curve measurements of leakage current, and matching with model predictions to extract and refine estimates for key parameters. The model will then be used to predict results that can be compared against experiment. Ultimately the validated model may be used for parameter exploration and optimization. A concurrent effort is to seek corroboration with estimates from first principles quantum mechanical (QM) and molecular dynamics (MD) calculations of trap depths and metal-polymer barrier potentials.

Acknowledgement

Support by the Department of the Navy, Office of Naval Research, grant N000141310064, is gratefully acknowledged.

References

[1] P. Barber, S. Balasubramanian, Y. Anguchamy, S. Gong, A. Wibowo, A., H. Gao, H.J. Ploehn, H-C. zur Loye, Polymer composite and nanocomposite dielectric materials for pulse power energy storage. Materials, **2**(2009) 1697-1733.

[2] M. Poulsen, S. Ducharme, Why ferroelectric Polyvinylidene Fluoride is special. IEEE Trans. Diel. Elec. Ins., **17**(2010) 1028-1035.

[3] J. Li, S.I. Seok, B. Chu, F. Dogan, Q. Zhang, Q. Wang,. Nanocomposites of ferroelectric polymers with TiO2 nanoparticles exhibiting significantly enhanced electrical energy density. Adv. Mater., **21**(2009) 217-221.

[4] M.N. Almadhoun, U.S. Bhansali, H.N. Alshareef, Nanocomposites of ferroelectric polymers with surface-hydroxylated $BaTiO_3$ nanoparticles for energy storage applications. J. Mater. Chem., **22**(2012) 11196-11200.

[5] O. Gallot-Lavallee, V. Griseri, G. Teyssedre, C. Laurent, The pulse electroacoustic technique in research on dielectric for electrical engineering. RIGE, **8**(2005) 749-772.

[6] G.M. Sessler, J.E. West, G. Gerhard, High-resolution laser pulse method for measuring charge distribution in dielectrics. Phys. Rev. Lett., **48**(1982) 560-563.

[7] I. Boukhris, E. Belgaroui, A. Kallel, Physical and numerical modeling for bipolar charge transport in disordered polyethylene under high DC voltage. Int. J. Elec. Eng. Informatics, **2**(2010) 313-324.

[8] G. Chen, S.H. Loi, Space charge modeling in solid dielectrics under high electric field based on double charge injection model. MRS Fall Meeting, 2006.

[9] M.H. Lean, W-P.L. Chu, Dynamic charge mapping in layered polymer films. IEEE Trans. Diel. Elec. Ins., **21**(2014) 1319-1329.

[10] R. Mekala, N. Badi, Modeling and simulation of high permittivity core-shell ferroelectric polymers for energy storage solutions. Proc. 2013 COMSOL Conference, Boston.

[11] I.A. Tsekmes, R. Kochetov, P.H.F. Morshuis, J.J. Smit, T. Andritsch, Modeling the dielectric response of epoxy based nanocomposites. Proc. IEEE Elec. Ins. Conf. 2014, 47-50.

[12] M.H. Lean, W-P.L. Chu, Effect of gaseous void on bipolar charge transport in layered polymer film. J. Phys. D: Appl. Phys., **47**(2014) 075303.

[13] M.H. Lean, W-P.L. Chu, Simulation of charge packet formation in layered polymer film. COMPEL: Int. J. Comp. Math. Elec. & Elec. Eng., **33**(2014) 1396-1415.

[14] D. Pisa, M.G. Danikas, Interfaces features in polymer nanocomposites: a review of proposed models. NANO: Brief Reports and Reviews, **6**(2011) 497-508.

[15] M.H. Lean, W-P.L. Chu, Dielectric breakdown model for polymer films. IEEE Trans. Diel. Elec. Ins., **21**(2014) 2259-2266.

[16] R.W. Hockney, J.W. Eastwood, Computer Simulation Using Particles, McGraw-Hill, New York, 1981.

[17] J.M. Dawson, Particle simulation of plasmas. Rev. Mod. Phys., **55**(1983) 403-447.

[18] C.K. Birdsall, Particle-in-cell charged-particle simulations, plus Monte Carlo collisions with neutral atoms, PIC-MCC. IEEE Trans. on Plasma Sci., **19**(1991) 65-85.

[19] S. Gottlieb, C.W. Shu, E. Tadmor, Strong stability-preserving high-order time discretization methods. SIAM Rev., **43**(2001) 89-112.

[20] D.M. Caughey, R.E. Thomas, Carrier mobilities in silicon empirically related to doping and field. Proc. IEEE, **55**(1967) 2192-2193.

[21] C. Duan, W.N. Mei, W. Yin, J. Liu, J.R. Hardy, S. Ducharme, P.A. Dowben, Simulations of ferroelectric polymer film polarization: The role of dipole interactions. Phys. Rev. B, **69**(2004) 235106.

[22] M.H. Lean, W-P.L. Chu, Simulation of bipolar charge transport in nanocomposite polymer films. J. Appl. Phys., **117**(2015) 104102.

[23] M.H. Lean, W-P.L. Chu, Model for charge transport in ferroelectric nanocomposite films. J. Polymers, **2015**(2015) 745056.

[24] Y. Yuan, P. Sharma, Z. Xiao, S. Poddar, A. Gruverman, S. Ducharme, J. Huang,. Understanding the effect of ferroelectric polarization on power conversion efficiency of organic photovoltaic devices. Energy Environ. Sci., **5**(2012) 8558-8563.

[25] D.R. Paul, L.M. Robeson, Polymer nanotechnology: Nanocomposites, Polymer, **49**(2008**)** 3187-3204.